Eur. Phys. J. C (2025) 85:930
https://doi.org/10.1140/epjc/s10052-025-14665-1

THE EUROPEAN PHYSICAL JOURNAL C

Regular Article - Theoretical Physics

Probing stability of dark matter sustained wormholes in matter-curvature coupled gravity

Zinnat Hassan[1,a], **Aaqid Bhat**[2,b], **P. K. Sahoo**[2,c]

[1] Department of Mathematics, School of Arts, Sciences, Humanities and Education, SASTRA Deemed University, Trichy-Tanjore Road, Thirumalaisamudram, Thanjavur, Tamil Nadu 613401, India
[2] Department of Mathematics, Birla Institute of Technology and Science, Pilani, Hyderabad Campus, Jawahar Nagar, Kapra Mandal, Medchal District, Telangana 500078, India

Received: 8 July 2025 / Accepted: 21 August 2025

Abstract We investigate traversable wormhole solutions sustained by dark matter in the context of curvature-matter coupled gravity, specifically the $f(R, \mathcal{L}_m, T)$ theory. By analyzing the traversability criteria, we identify constraints on the model parameters that ensure physically viable, asymptotically flat wormhole geometries. Our results show that while small values of the dark matter density ρ_s preserve asymptotic flatness, larger values of the coupling parameter β may violate the flare-out condition. Furthermore, we find that the null energy condition is violated near the throat $r = r_0$, indicating the effective role of the modified gravity terms as a source of exotic matter. To examine the stability and physical possibility of the solutions, we perform a comprehensive analysis involving gravitational lensing, the complexity factor, the anisotropy parameter, active gravitational mass, total gravitational energy, and the volume integral quantifier. Our findings demonstrate that stable, traversable wormholes can emerge within specific parameter regimes in this framework with minimal exotic matter, offering new insights into the interplay between dark matter and modified gravity.

1 Introduction

Wormholes serve as theoretical passages that connect two separate universes or distant regions within the same universe. The idea was initially introduced by Einstein and Rosen in 1935 through their well-known Einstein–Rosen bridge [1]. However, the term "wormhole" was later coined by Misner and Wheeler in 1957 [2]. It was not until 1988 that Morris and Thorne [3,4] successfully explored an exact solution to the Einstein field equations for traversable wormholes. Their study revealed that the energy-momentum tensor associated with such wormholes inevitably violates the null energy condition (NEC) [3,5], which is the weakest among the classical energy conditions and, consequently, leads to the violation of all others. This means that maintaining a traversable wormhole requires a form of matter with negative energy density, often referred to as exotic matter. A well-known example of such a solution in General Relativity (GR) is the Ellis wormhole [6–8]. However, in modified gravity theories, the necessity for exotic matter is significantly reduced, making the construction of traversable wormholes more feasible. The investigation of wormhole geometries has gained significant attention within the context of various modified theories of gravity. Notably, traversable wormhole solutions have been studied in several extended frameworks, including higher-dimensional GR [9,10], non-symmetric gravitational theories [11], and Einstein–Gauss–Bonnet gravity [12,13]. Additional progress has been made in the context of Einstein–Cartan theory [14,15], models with curvature-matter coupling [16,17], and Rastall gravity [18–20], among other alternative approaches [21–27]. These works suggest that the incorporation of extended geometric structures or modified matter couplings can reduce or eliminate the dependency on exotic matter, thereby enabling the existence of stable and traversable wormhole solutions within these frameworks.

Recently, Haghani and Harko [28] proposed a novel extension of gravitational theory that incorporates a coupling between geometry and matter, known as $f(R, \mathcal{L}_m, T)$ gravity. This framework serves as a unifying model that encompasses and extends several well-known modified theories of gravity, including $f(R)$, $f(R, T)$, and $f(R, \mathcal{L}_m)$. By inte-

[a] e-mail: zinnathassan980@gmail.com (corresponding author)
[b] e-mail: aaqid555@gmail.com
[c] e-mail: pksahoo@hyderabad.bits-pilani.ac.in

Published online: 01 September 2025

grating the Lagrangian density of matter $\mathcal{L}_m$ and the trace of the energy-momentum tensor T into the gravitational action, this theory provides a more prosperous structure to explore matter-geometry interactions. Further developments, particularly the Palatini formulation of $f(R, \mathcal{L}_m, T)$ gravity, have been explored in detail in [29]. Also, in [30], the author investigated the late-time accelerating cosmological models with observational constraints in modified $f(R, \mathcal{L}_m, T)$ gravity. In addition, the causality problem and its violation in $f(R, \mathcal{L}_m, T)$ gravity were discussed in [31]. In the context of compact objects, Moraes et al. [32] investigated and obtained wormhole solutions in $f(R, \mathcal{L}_m, T)$ gravity. In [33], the authors analyzed the impact of non-commutative geometry on the formation and stability of wormholes in this modified gravity theory. Further, wormhole solutions with Einstein clusters as dark matter model have been discussed in [34]. Recently, quasinormal modes of Casimir wormholes with GUP corrections in the context of $f(R, \mathcal{L}_m, T)$ gravity have been discussed in [35]. Since the application of this gravity theory in astrophysical contexts remains relatively not much explored, our study aims to contribute by examining wormhole solutions sustained by some dark matter (DM) models within the $f(R, \mathcal{L}_m, T)$ gravity framework. This study provides insights into the role of DM in shaping the structure and characteristics of wormholes in the context of modified gravity. To achieve this, we adopt a simple model, $f(R, \mathcal{L}_m, T) = R + \alpha\mathcal{L}_m + \beta T$, where α and β are model parameters. A key advantage of this formulation is that it allows for direct comparisons with other gravitational models, such as $f(R, T)$ and $f(R, \mathcal{L}_m)$, alongside Einstein's GR. In particular, setting $\alpha = \beta = 0$ recovers the GR case, while $\alpha = 0$ corresponds to the $f(R, T)$ model, and $\beta = 0$ leads to the $f(R, \mathcal{L}_m)$ model. This setup makes it easier to compare different gravity theories and helps us to clearly see how geometry-matter coupling affects the wormhole structure.

Based on the standard cosmological model and recent observational findings, the universe is composed of roughly 4% atomic matter, 29.6% dark matter, and 67.4% dark energy [36,37]. At the galactic level, DM significantly influences the formation and evolution of galaxies [38]. The idea of dark matter was first introduced by Zwicky, who applied the virial theorem to suggest its existence [39]. Spiral galaxies are believed to follow Universal Rotation Curves (URC), and the presence of DM in galactic halos can be inferred from its gravitational influence on these rotation curves [40,41]. Given the widespread presence of DM halos in galaxies, studying the formation of traversable wormholes within these environments becomes highly relevant (see, e.g., [42,43]). Some studies, such as [42], suggest that traversable wormholes could form in the outer halos of galaxies based on the Navarro–Frenk–White (NFW) profile. Another perspective on DM described by a pseudo-isothermal (PI) profile is associated with alternative gravitational theories, such as Modified Newtonian Dynamics (MOND) [44]. MOND challenges the conventional DM hypothesis by attributing galactic mass distribution discrepancies to Newtonian dynamics modifications at low accelerations rather than the presence of unseen matter [45–47]. Several studies have demonstrated the effectiveness of the PI profile in accounting for galactic observations. For example, de Blok et al. [48] conducted a comparative analysis between the PI and NFW models and found that the PI profile, characterized by its flat central core, provides a superior fit to the observed density distributions of low surface brightness galaxies. This feature makes the PI model a promising solution to the well-known "core-cusp problem". Furthermore, Paul [49] explored the possibility of traversable wormholes in the context of MOND, both with and without coupling to a scalar field, highlighting the viability of such geometries. In recent years, we can see a large number of papers on wormhole geometry with different dark matter models, for instance, Refs. [50–53].

In this paper, we consider an anisotropic fluid configuration, where the radial and tangential pressures are not equal. This choice is not merely a mathematical generalization but is deeply rooted in the physics of self-gravitating systems. In compact objects, local pressure isotropy is an idealized condition that rarely holds. A wide range of physical phenomena, such as the presence of strong magnetic fields, viscous stresses, phase transitions, superfluidity, pion condensation, and local anisotropic velocity distributions, can give rise to pressure anisotropies within stellar interiors and dense matter configurations. These mechanisms and their implications for relativistic stellar models are extensively reviewed in the literature, particularly by Herrera and Santos [54], where the authors provide a detailed account of various sources of anisotropy and their role in the equilibrium and stability of compact objects. Moreover, the emergence of anisotropy can be viewed as a natural outcome of the dynamical evolution of relativistic fluid systems. Herrera [55] has demonstrated that physical processes expected during the evolution of astrophysical objects, such as dissipative effects (e.g., heat flow, radiation, shear viscosity), automatically lead to anisotropic pressure, even if the system initially starts in an isotropic state. Importantly, the anisotropy developed during this dynamical phase does not necessarily disperse once the system reaches equilibrium. Thus, the final equilibrium configuration of a self-gravitating system is expected to exhibit pressure anisotropy.

In the context of wormhole geometries, the inclusion of anisotropic matter becomes even more crucial. Anisotropic fluids provide essential flexibility in satisfying the geometric requirements of traversable wormholes, particularly the flaring-out condition at the throat and the associated energy condition violations. Numerous studies have shown that anisotropic matter sources enable the construction of

traversable wormholes with better physical behavior in both GR and modified gravity theories (see some Refs. [56–60]). Consequently, incorporating anisotropic pressure in our wormhole solutions is both physically motivated and essential for capturing realistic features of dense gravitational systems.

This paper explores wormhole solutions within the framework of three DM models: URC, NFW, and PI models. We shall conduct a comparative analysis of these models on wormhole geometry in the context of $f(R, \mathcal{L}_m, T)$ gravity. The structure of the paper is organized as follows: Sect. 2 provides an overview of $f(R, \mathcal{L}_m, T)$ gravity and presents the corresponding field equations for wormholes. In Sect. 3, we discuss the DM profiles and derive the associated wormhole solutions, whereas in Sect. 4, energy conditions are discussed. Section 5 focuses on analyzing the stability of wormhole solutions influenced by these DM models. Finally, we summarize our findings and present conclusions in Sect. 6.

2 Field equations in $f(R, \mathcal{L}_m, T)$ gravity

The general static, spherically symmetric Morris–Thorne metric [3] can be defined as

$$ds^2 = -e^{2\Phi(r)}dt^2 + \frac{dr^2}{1 - b(r)/r} + r^2(d\theta^2 + \sin^2\theta d\phi^2), \tag{1}$$

where $\Phi(r)$ is the redshift function, responsible for the gravitational redshift. To ensure the absence of event horizons, $\Phi(r)$ must remain finite throughout spacetime. The function $b(r)$, known as the shape function, determines the geometry of the wormhole and must satisfy certain conditions. The first condition is the flare-out condition, which plays a crucial role in ensuring that a wormhole remains traversable. Mathematically, this condition is expressed as [3]

$$\frac{b - b'r}{b^2} > 0. \tag{2}$$

At the wormhole throat, this expression simplifies to

$$b'(r_0) < 1. \tag{3}$$

Moreover, for any region beyond the throat ($r > r_0$), the inequality

$$1 - \frac{b(r)}{r} > 0 \tag{4}$$

must hold to maintain an open wormhole structure. Additionally, the wormhole should exhibit asymptotic flatness, i.e.,

$$\frac{b(r)}{r} \to 0 \quad \text{as} \quad r \to \infty. \tag{5}$$

Now, we introduce the gravitational action functional [28]

$$\mathcal{S} = \frac{1}{16\pi}\int [f(R, \mathcal{L}_m, T) + \mathcal{L}_m]\sqrt{-g}\, d^4x. \tag{6}$$

Here, $\mathcal{L}_m$ denotes the matter-Lagrangian density, and R is the Ricci scalar. Now, varying the action (6) corresponding to $g_{\mu\nu}$ yields

$$f_R R_{\mu\nu} - \frac{1}{2}\left[f - (f_{\mathcal{L}_m} + 2f_T)\mathcal{L}_m\right]g_{\mu\nu} + \left(g_{\mu\nu}\Box - \nabla_\mu\nabla_\nu\right)$$
$$f_R = \left[8\pi + \frac{1}{2}(f_{\mathcal{L}_m} + 2f_T)\right]T_{\mu\nu} + f_T\tau_{\mu\nu} \tag{7}$$

where, $f_R = \frac{\partial f}{\partial R}$, $f_{\mathcal{L}_m} = \frac{\partial f}{\partial \mathcal{L}_m}$, $f_T = \frac{\partial f}{\partial T}$ and $\tau_{\mu\nu} = 2g^{\alpha\beta}\frac{\partial^2 \mathcal{L}_m}{\partial g^{\mu\nu}\partial g^{\alpha\beta}}$. Additionally, $T_{\mu\nu}$ represents the energy-momentum tensor, and its standard form is given by

$$T_{\mu\nu} = \frac{-2}{\sqrt{-g}}\frac{\delta(\sqrt{-g}\mathcal{L}_m)}{\delta g^{\mu\nu}}. \tag{8}$$

In this paper, we consider an anisotropic energy-momentum tensor described by

$$T^{\mu}_{\ \nu} = \text{diag}(-\rho, p_r, p_t, p_t), \tag{9}$$

where ρ denotes the energy density of the matter distribution, and p_r and p_t represent the radial and tangential pressures, respectively. For a gravitational Lagrangian with an additive structure given by $f(R, \mathcal{L}_m, T) = R + \alpha\mathcal{L}_m + \beta T$ [28,35], where α and β are constant parameters and assuming $\mathcal{L}_m = -\rho$, the field equations (7) simplify to

$$G_{\mu\nu} = \left(8\pi + \frac{\alpha}{2} + \beta\right)T_{\mu\nu} + \frac{\beta}{2\rho + T}g_{\mu\nu}. \tag{10}$$

Now, we solve Eqs. (1), (9), and (10), and obtain the field equations under constant redshift function

$$\frac{b'}{r^2} = \rho\left(\lambda - \frac{\beta}{2}\right) - \frac{\beta}{2}(p_r + 2p_t), \tag{11}$$

$$-\frac{b}{r^3} = p_r\left(\lambda + \frac{\beta}{2}\right) + \frac{\beta}{2}(2p_t + \rho), \tag{12}$$

$$\frac{1}{2r^2}\left(\frac{b}{r} - b'\right) = p_t(\lambda + \beta) + \frac{\beta}{2}(p_r + \rho), \tag{13}$$

where $\lambda = \left(8\pi + \frac{\alpha}{2} + \beta\right)$. Now, with the above field equations, we shall study the effect of DM models on wormhole geometry.

3 Wormhole configurations through dark matter profiles

This study explores various critical aspects of DM halos, with a particular focus on galactic wormholes inferred from rotation curve analyses [43,61]. The idea of DM originated from studies on Oort constants [62] and investigations into

galaxy cluster masses [39,63], a researcher sought to explain the observed flat rotation curves. To model this phenomenon, the NFW density profile [64,65] was developed, along with the Einasto profile, which has shown improved precision in certain simulations of DM halo [66,67]. In general, wormhole throats are often embedded within various types of DM halos, and deviations from standard energy conditions provide evidence of their existence. In this section, we examine various representations of DM halos and explore wormhole solutions within different DM profiles. We shall use the following DM models for this study

$$\rho(r)=\begin{cases}\frac{\rho_s\, r_s^3}{(r+r_s)(r^2+r_s^2)}, & \text{(URC model)}\\ \frac{\rho_s}{(r/r_s)(1+r/r_s)^2}, & \text{(NFW model)}\\ \frac{\rho_s}{1+\left(\frac{r}{r_s}\right)^2}, & \text{(PI model)}\end{cases} \tag{14}$$

3.1 $\rho(r)=\frac{\rho_s\, r_s^3}{(r+r_s)(r^2+r_s^2)}$

As the first case, we consider the Burkert halo profile, which is now widely referred to as the universal rotation curve (URC) profile, defined as [68]

$$\rho(r)=\frac{\rho_s\, r_s^3}{(r+r_s)(r^2+r_s^2)}, \tag{15}$$

where r_s and ρ_s denote the core radius and central density of the dark matter halo, respectively. Combined with appropriate baryonic, gaseous, and stellar components, this profile successfully reproduces the observed kinematics of disk galaxies [69]. Moreover, it generates disc mass estimates that are consistent with those predicted by stellar population synthesis models [70–73]. One notable advantage of the Burkert profile is its ability to approximate the NFW velocity profiles at small radii for suitable choices of r_s, and it asymptotically approaches the NFW profile for $r > 0.3\, R_{\rm vir}$. Thus, the rotation curve data themselves constrain the value of the best-fit parameter r_s, offering a measure of the halo's central cuspiness. Further, Persic et al. [74], through their analysis of H_α data along with several radio rotation curves, identified a large set of rotation curve profiles. Their results demonstrate that these curves can be consistently modeled across a broad range of luminosities and galaxy morphologies, including spiral galaxies, low-surface-brightness ellipticals, and dwarf irregulars. As a result, they introduced the term "universal rotation curve" (URC) to replace the conventional notion of "rotation curves," highlighting the wide-ranging applicability of this observed feature.

Now, we shall compare the URC energy density (15) with the obtained energy density of wormholes under $f(R,\mathcal{L}_m,T)$, and obtain the shape function, given by

$$b(r)=\frac{1}{2}\rho_s r_s^3\Lambda_1\left[\frac{1}{4}\log\left(r_s^2+r^2\right)+\frac{1}{2}\log(r_s+r)-\frac{1}{2}\tan^{-1}\left(\frac{r}{r_s}\right)\right]+c_1, \tag{16}$$

where $\Lambda_1=(\alpha+2\beta+16\pi)$. Now, applying throat condition $b(r_0)=r_0$, we get

$$b(r)=r_0+\frac{1}{8}\rho_s r_s^3\Lambda_1\left[\Lambda_2+2\Lambda_3-2\Lambda_4\right], \tag{17}$$

where,

$$\Lambda_2=\log\left(r_s^2+r^2\right)-\log\left(r_s^2+r_0^2\right), \tag{18}$$

$$\Lambda_3=\log(r_s+r)-\log(r_s+r_0), \tag{19}$$

$$\Lambda_4=\tan^{-1}\left(\frac{r}{r_s}\right)-\tan^{-1}\left(\frac{r_0}{r_s}\right). \tag{20}$$

Also, the expression for $b(r)$ follows the asymptotic condition, i.e., $\frac{b(r)}{r}\to 0$ as $r\to\infty$. Further, the flare-out condition at $r=r_0$, can be read as

$$b'(r)\mid_{r=r_0}=\frac{\rho_s r_s^3 r_0^2\Lambda_1}{2(r_s+r_0)\left(r_s^2+r_0^2\right)}, \tag{21}$$

which satisfies for $\rho_s=0.004\,\text{kpc}^{-2}$, $r_s=2\,\text{kpc}$ [75].

3.2 $\rho(r)=\frac{\rho_s}{(r/r_s)(1+r/r_s)^2}$

An approximate analytical representation of the NFW density profile is derived based on the Cold Dark Matter (ΛCDM) paradigm and supported by high-resolution numerical simulations [64,65,76]. This profile effectively characterizes the dark matter halo structures on galactic and cluster scales and is given by

$$\rho(r)=\frac{\rho_s}{(r/r_s)\,(1+r/r_s)^2}, \tag{22}$$

where ρ_s denotes the characteristic density at the time of halo formation, and r_s represents the scale radius that distinguishes the transition between the inner and outer regions of the halo. In the inner region, the density behaves as $\rho(r)\propto r^{-1}$, forming a central cusp, while at larger radii it falls off as $\rho(r)\propto r^{-3}$ [64]. The NFW profile demonstrates a remarkable ability to fit halos over a wide mass range, from dwarf galaxies to massive galaxy clusters. Despite its widespread applicability, the NFW profile faces a significant limitation, known as the "core-cusp problem", where the steep central density predicted by the model is inconsistent with the nearly flat density cores observed in many low-mass galaxies [65]. Further refinements have been proposed to address such discrepancies. For instance, Navarro et al. [65] improved the profile through advanced simulations, reinforcing its general effectiveness and emphasizing deviations in the central regions of halos. Further, in response to these issues, alternative models such as the Einasto profile have been introduced, offering additional flexibility through

an extra shape parameter to better accommodate observed inner halo structures [67]. Moreover, baryonic mechanisms, including supernova-driven winds and activity from central black holes, significantly modify the central density, potentially softening the inner cusp and improving alignment with observational data [77]. Nevertheless, the NFW profile remains a widely adopted model due to its simplicity and predictive power, especially in studies involving smaller halos such as dwarf galaxies [78].

Following the previous methodology, we can easily calculate the shape function for this case, which can be read as

$$b(r) = \frac{1}{2}\rho_s r_s^3 \Lambda_1 \left(\frac{r_s}{r_s + r} - \frac{r_s}{r_s + r_0} + \Lambda_3\right) + r_0, \tag{23}$$

where we have imposed the throat condition $b(r_0) = r_0$. The flare-out condition for this case can be obtained at the throat

$$b'(r) = \frac{1}{2}\rho_s r_s^3 \Lambda_1 \left(\frac{1}{r_s + r} - \frac{r_s}{(r_s + r)^2}\right) < 1, \quad \text{at} \quad r = r_0. \tag{24}$$

3.3 $\rho(r) = \frac{\rho_s}{1+\left(\frac{r}{r_s}\right)^2}$

In addition to the commonly used URC and NFW dark matter profiles, another significant variety of models emerges from the framework of modified theories, such as the MOND paradigm [44]. Within this context, the PI profile often characterizes the dark matter distribution, which provides a well-behaved density function at the galactic center. The PI density profile is given by

$$\rho_{\rm PI} = \frac{\rho_s}{1 + \left(\frac{r}{r_s}\right)^2}, \tag{25}$$

where ρ_s denotes the central density of the dark matter halo, and r_s is the corresponding scale radius. Unlike the NFW profile, which features a central cusp with a steep rise in density, the PI profile exhibits a core-like behavior with a flat central density, aligning more closely with observational data from low surface brightness (LSB) and dwarf galaxies. The PI profile has been widely recognized for its success in addressing the "core-cusp problem", a key limitation of the NFW model. De Blok et al. [48] performed a comparative analysis of the NFW and PI profiles and concluded that the flat-core structure of the PI model better represents the observed density distributions in LSB galaxies. Similarly, Gentile et al. [70] demonstrated that the PI profile yields consistent fits to the rotation curves of spiral galaxies across various radial distances, reinforcing its empirical validity. Oh et al. [79] further validated the effectiveness of the PI model in dwarf galaxy systems using data from the THINGS survey, where accurate representations of dark matter distributions were achieved without requiring fine-tuning. Beyond observational applications, the PI profile has also been examined in the theoretical context of wormhole geometries. In particular, Ref. [80] investigated the dark matter density associated with axisymmetric traversable wormholes and found that it mirrors the behavior of black hole density spikes. Interestingly, the dark matter density profile exhibits spin dependence, varying oppositely with the wormhole's angular momentum. These findings underscore the versatility and relevance of the PI profile in both astrophysical modeling and theoretical frameworks, offering valuable insights into the structure and dynamics of dark matter in various gravitational scenarios.

The shape function for this case can be read as

$$b(r) = -\frac{1}{2}\rho_s r_s^3 \Lambda_1 \Lambda_4 + \frac{1}{2}\rho_s r_s^2 \Lambda_1 (r - r_0) + r_0, \tag{26}$$

and in the limit $r \to \infty$, the asymptotic condition $\frac{b(r)}{r} \to 0$ is satisfied. Further, we checked the flare-out condition at the throat, i.e.,

$$b'(r_0) = \frac{(\alpha + 16\pi + 4)\rho_s r_s^2 r_0^2}{2\left(r_s^2 + r_0^2\right)} \tag{27}$$

Now, we analyze the behavior of the shape function for each case. In the limit $r \to \infty$, the asymptotic condition $\frac{b(r)}{r} \to 0$ is satisfied for the parameters $\rho_s = 0.004\,\text{kpc}^{-2}$, $r_s = 2\,\text{kpc}$ [75], $r_0 = 1$ along with any values of the model parameters α and β. However, for large values of ρ_s and r_s, this condition will no longer be valid. Furthermore, we evaluated the flare-out condition in the throat for each case and plotted the corresponding graphs in Fig. 1. Our analysis confirms that the flare-out condition holds for parameters $\rho_s = 0.004\,\text{kpc}^{-2}$, $r_s = 2\,\text{kpc}$ [75], and the radius of the throat $r_0 = 1$. For comparison, we have included graphs for GR ($\alpha = 0 = \beta$), $f(R, T)$ gravity ($\alpha = 0$, $\beta = 1$) and $f(R, \mathcal{L}_m, T)$ gravity ($\alpha = 1, 2$; $\beta = 1, 2$). The deviations in the graphs become evident as the model parameters vary. In particular, the parameter β has a more significant influence on the shape function compared to α. We also note that for higher values of β, the properties of the shape function fail, especially the flare-out condition. Now, with these obtained solutions, we shall study some significant features of the wormhole geometry, such as the energy conditions, deflection angles of wormholes, complexity factor, anisotropy parameter, active gravitational mass, and total gravitational energy, along with the emergence of exotic matter through the VIQ equation.

4 Energy conditions

In this section, we aim to explore the geometric structure of the derived wormhole solutions through the lens of energy conditions. These conditions impose constraints on the stress-energy tensor $T_{\mu\nu}$, which governs the distribution of matter and energy in spacetime. Building on our earlier

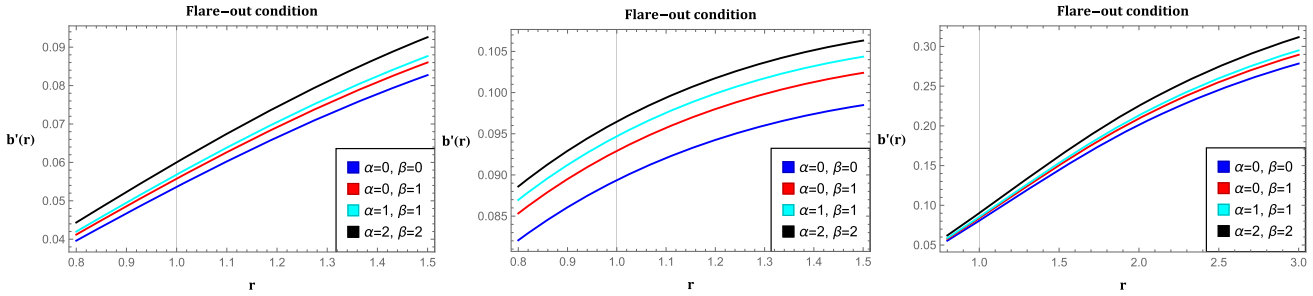

(a) URC (b) NFW (c) PI

Fig. 1 Plots for the flare-out condition of the shape functions against the radial coordinate r. The blue line represents the GR case, the red line shows the $f(R,T)$ gravity case, and the cyan and black represent the $f(R,\mathcal{L}_m,T)$ case. We consider the parameter values $\rho_s = 0.004\,\mathrm{kpc}^{-2}$, $r_s = 2\,\mathrm{kpc}$, and the throat radius $r_0 = 1$

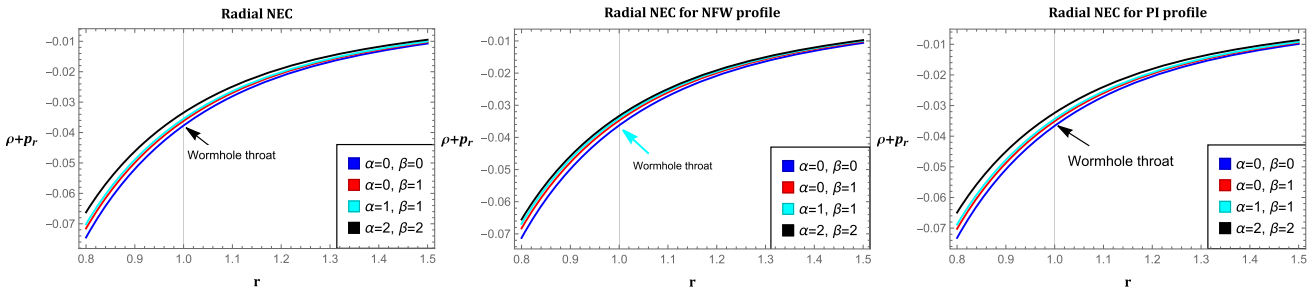

(a) URC (b) NFW (c) PI

Fig. 2 Plots for the NEC against the radial coordinate r. The blue line represents the GR case, the red line shows the $f(R,T)$ gravity case, and the cyan and black represent the $f(R,\mathcal{L}_m,T)$ case. We consider the parameter values $\rho_s = 0.004\,\mathrm{kpc}^{-2}$, $r_s = 2\,\mathrm{kpc}$, and the throat radius $r_0 = 1$

results, we now examine the validity of various energy conditions, particularly focusing on the NEC, and present our findings through graphical analysis. the NEC is expressed as $T_{\mu\nu}k^\mu k^\nu \geq 0$, which, in component form

$$\rho + p_i \geq 0, \quad \text{where } i = r \text{ or } t. \tag{28}$$

where k^μ represents a null vector. Within the framework of GR, the requirement for a wormhole to be traversable, namely, the flaring-out condition, which leads to $G_{\mu\nu}k^\mu k^\nu < 0$, which, via Einstein's field equations, implies $T_{\mu\nu}k^\mu k^\nu < 0$, thereby violating the NEC. Assuming the stress-energy tensor of the form provided in Eq. (9), this violation becomes evident. However, this scenario changes significantly in the realm of modified theories of gravity. In such frameworks, the effective energy-momentum tensor includes not only the usual matter contributions but also additional terms arising from the modified gravitational sector. As a result, the apparent violation of NEC may be attributed to these extra geometric contributions rather than the matter content alone. For example, one can check the literature where wormhole solutions have been obtained by satisfying the energy conditions [81–83]. Here, we study the behavior of NEC for the solutions obtained for the shape functions.

For the URC model, considering the Eqs. (11–13), (15), and (17), we can easily obtain the expressions for NEC

$$\rho + p_r = \frac{\rho_s r_s^3}{(r_s + r)\left(r_s^2 + r^2\right)} + \frac{\rho_s r_s^3}{4r^3}\left(-\Lambda_2 - 2\Lambda_3 + 2\Lambda_4\right) - \frac{2r_0}{r^3\Lambda_1}, \tag{29}$$

Also, the NEC for the NFW case can be read as

$$\rho + p_r = \frac{1}{r^3}\left[\rho_s r_s^3\left(\Lambda_3 + \frac{-r_s^2 - r_s r + r^2}{(r_s + r)^2} + \frac{r_s}{r_s + r_0}\right) - \frac{2r_0}{\Lambda_1}\right]. \tag{30}$$

Similarly, the NEC for the PI case

$$\rho + p_r = \frac{\rho_s r_s^2}{r_s^2 + r^2} + \frac{1}{r^3}\left[\rho_s r_s^2\left(r\Lambda_4 + r_0 - r\right) - \frac{2r_0}{\Lambda_1}\right] \tag{31}$$

At $r = r_0$, the radial NEC for all cases can be read as

$$\rho + p_r|_{r=r_0} = \begin{cases} \frac{\rho_s r_s^3}{(r_s+r_0)(r_s^2+r_0^2)} - \frac{2}{r_0^2\Lambda_1}, & \text{(URC)} \\ \frac{1}{r_0^2}\left[\frac{\rho_s r_s^3 r_0}{(r_s+r_0)^2} - \frac{2}{\Lambda_1}\right], & \text{(NFW)} \\ \frac{\rho_s r_s^2}{r_s^2+r_0^2} - \frac{2}{r_0^2\Lambda_1}, & \text{(PI)} \end{cases} \tag{32}$$

By analyzing the above expressions in Eq. (32) and substituting the specific parameter values obtained in the previous section, we find that the R.H.S. is a negative quantity. This confirms that the NEC is violated at the throat (for a graphical representation, see Fig. 2). Since the violation of NEC implies the breakdown of all other energy conditions, it indicates that the wormhole is not supported by ordinary matter but rather by non-standard gravitational interactions. In other words, exotic matter is required to sustain the wormhole structure and prevent its collapse. However, in this case, the violation arises due to the effects of modified gravity, which effectively acts as an alternative source of exotic matter near the throat.

5 Investigating the stability of the wormhole solutions

In this section, we shall study the stability of the obtained solutions through various parameters such as weak gravitational lensing, complexity factor, anisotropy parameter, active gravitational mass, total gravitational energy, and volume integral quantifier methods.

5.1 Deflection angles of wormholes

Now, we apply the Gauss–Bonnet theorem (GBT) to determine the deflection angle caused by gravitational lensing. Let $\mathcal{A}_R$ represent a smooth, connected region enclosed by a circular curve γ_R and a geodesic path $\gamma_{\bar{g}}$, such that $\partial\mathcal{A}_R = \gamma_R \cup \gamma_{\bar{g}}$, where $\bar{g}$ is the optical metric. Here, κ_g represents the geodesic curvature, and K indicates the Gaussian curvature. Further, the GBT establishes a vital connection between geometry and topology by expressing the following relation [84]

$$\iint_{\mathcal{A}_R} K dS + \oint_{\partial\mathcal{A}_R} \kappa_g dt + \sum_i \theta_i = 2\pi\chi(\mathcal{A}_R). \tag{33}$$

Here, θ_i represents the exterior angles at the vertices, dS represents the optical surface element, and $\chi(\mathcal{A}_R)$ is the Euler characteristic of the surface $\mathcal{A}_R$. Since the geodesic curvature along $\gamma_{\bar{g}}$ is zero, the boundary contribution to the integral arises solely from γ_R, where the geodesic curvature is given by

$$\kappa_g(\gamma_R) = |\nabla_{\dot{\gamma}_R}\dot{\gamma}_R|. \tag{34}$$

Defining γ_R as a constant-radius curve $r(\phi) = R$, and along with the unit speed condition, it follows that as $R \to \infty$, the geodesic curvature approaches $1/R$. This leads to the relation

$$\lim_{R\to\infty} \kappa_g(\gamma_R)\frac{dt}{d\phi} = 1. \tag{35}$$

If we consider a sufficiently large distance, the addition of jump angles at the source S and the observer O satisfies $\theta_S + \theta_O \to \pi$. Based on this construction, the GBT results in

$$\lim_{R\to\infty}\left[\iint_{\mathcal{A}_R} K\, dS + \int_0^{\pi+\hat{\boldsymbol{\theta}}} \left(\kappa_g \frac{dt}{d\phi}\right)_{\gamma_R} d\phi\right] = \pi. \tag{36}$$

Therefore, the deflection angle of a light ray can be determined as

$$\hat{\boldsymbol{\theta}} = -\int_0^{\pi}\int_{r=\frac{\Psi}{\sin\phi}}^{\infty} K\, dS, \tag{37}$$

where Ψ represents the impact parameter. To compute the Gaussian curvature of the metric (1), we follow the method given in [84] and obtain

$$K = e^{2\Phi}\left(1 - \frac{b}{r}\right)\left[\Phi'' + \frac{\Phi'}{r} - \frac{rb' - b}{2r(r-b)}\left(\Phi' - \frac{1}{r}\right)\right]. \tag{38}$$

We now evaluate the Gaussian curvature and the deflection angles for each profile with constant gravitational redshift. For the URC model, the Gaussian curvature K_1 can be obtained as

$$K_1 \simeq \frac{\frac{1}{4}\rho_s r_s^3(-r_0)\Lambda_1 + \kappa_1 - 8r_0}{r^2} - \frac{\rho_s r_s^3\Lambda_1\log(r)}{4r^2} + \frac{\rho_s r_s^3}{4r} + \mathcal{O}\left(\frac{1}{r^3}\right), \tag{39}$$

where

$$\kappa_1 = \rho_s r_s^3\Lambda_1\left(-2\log(r_s + r_0) + 2\tan^{-1}\left(\frac{r_0}{r_s}\right) + \log(r_0)\right).$$

Here, we have approximated it in leading-order terms. Now with the above expression (39), the deflection angle of wormholes under the URC model can be rewritten as

$$\hat{\boldsymbol{\theta}}_{\mathbf{1}} = -\int_0^{\pi}\int_{r=\frac{\Psi}{\sin\phi}}^{\infty}\left[\frac{\frac{1}{4}\rho_s r_s^3(-r_0)\Lambda_1 + \kappa_1 - 8r_0}{r^2} + \frac{\rho_s r_s^3}{4r} - \frac{\rho_s r_s^3\Lambda_1\log(r)}{4r^2} + \mathcal{O}\left(\frac{1}{r^3}\right)\right] r\, dr\, d\phi. \tag{40}$$

Solving this integral, we find the following solution

$$\hat{\boldsymbol{\theta}}_{\mathbf{1}} \simeq -\frac{1}{4}\rho_s r_s^3\left(\pi - r_0\Lambda_1\log\left(\frac{2}{\Psi}\right)\right) - \frac{1}{4}\left(\rho_s r_s^3\Lambda_1\right) \times\left(-8\pi\log(r_s + r_0) + 8\pi\tan^{-1}\left(\frac{r_0}{r_s}\right) + 4\pi\log(r_0) - \pi\log(2)\right) + \frac{16r_0}{\Psi} + \mathcal{O}\left(\frac{1}{r^3}\right). \tag{41}$$

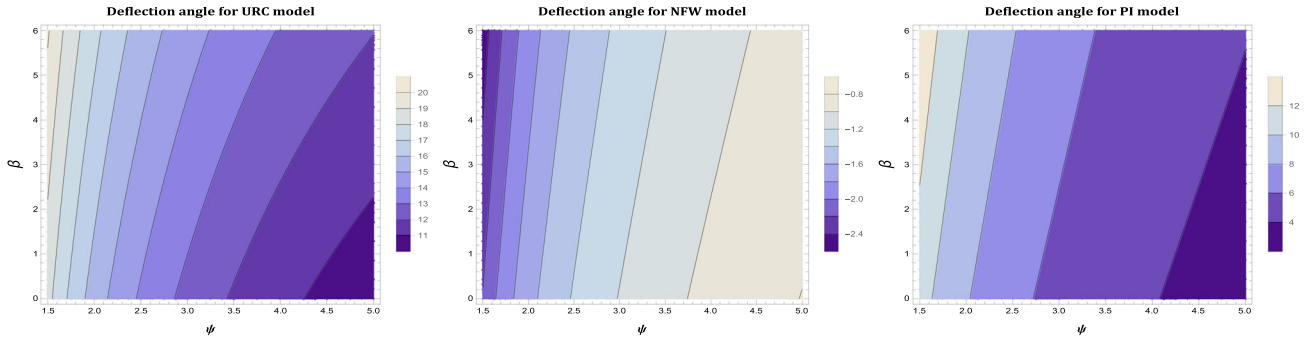

Fig. 3 The plots for the deflection angle against the impact parameter Ψ and the model parameter β. We consider the parameter values $\rho_s = 0.004\,\text{kpc}^{-2}$, $r_s = 2\,\text{kpc}$, throat radius $r_0 = 1\,\text{kpc}$ and $\alpha = 2$

Following the same procedure, we can calculate the deflection angle for the NFW model

$$\hat{\boldsymbol{\theta}}_{\mathbf{2}} \simeq \frac{\rho_s r_s^3}{18\Psi^3 r_0}\Big[(\Lambda_1\left(-9\Psi^2 r_s + 9\Psi^2 r_0(\log(2r_0) - \log(\Psi)) - 4r_s^2 r_0\right) - 144\pi\Psi^2 r_s + 18\pi^2\Psi r_s r_0\Big] \tag{42}$$

where the Gaussian curvature K_2 can be read as

$$K_2 \simeq \frac{AB^3\Lambda_1}{4r^2}\left(\frac{\log(r_0) - \log(r)}{r} - \frac{r_s}{r_0 + r} + \frac{r_s}{r^2} - \frac{2B^2}{r^3}\right) + \mathcal{O}\left(\frac{1}{r^4}\right). \tag{43}$$

Finally, for the PI case, the curvature K_3 can be obtained as

$$K_3 \simeq \frac{1}{4r^3}\left(\frac{\pi}{2}\rho_s r_s^3\Lambda_1 + \rho_s r_s^2 r_0\Lambda_1 - 2r_0\right) + \mathcal{O}\left(\frac{1}{r^4}\right), \tag{44}$$

and hence the deflection angle $\hat{\boldsymbol{\theta}}_{\mathbf{3}}$ is

$$\hat{\boldsymbol{\theta}}_{\mathbf{3}} \simeq \frac{\rho_s r_s^2\Lambda_1(\pi r_s + 2r_0) - 4r_0}{4\Psi} + \mathcal{O}\left(\frac{1}{\Psi^3}\right). \tag{45}$$

Now, we examine how light rays behave around the wormhole throat based on the approximate solutions obtained under different DM models. We have calculated the deflection angle $\hat{\boldsymbol{\theta}}$ up to the first three leading-order terms. The variation of the deflection angle as a function of Ψ and β is illustrated in Fig. 3. Our analysis reveals that both the model parameter β and the impact parameter Ψ significantly influence gravitational lensing. For the NFW case, we observe that when $\beta \in [0, 6]$, the deflection angle remains negative for all corresponding values of $\hat{\boldsymbol{\theta}}(\Psi)$. This suggests that photons experience a repulsive gravitational effect, causing light rays to bend outward rather than being drawn toward the wormhole. In contrast, for the URC and PI models, the deflection angle tends to be positive, indicating that light rays are instead bending inward toward the wormhole throat. Furthermore, as shown in Fig. 3, the deflection angle gradually approaches zero as the impact parameter increases indefinitely. This indicates that light rays traveling at large distances from the wormhole experience negligible gravitational effects and follow nearly straight paths. For further details on this topic, the readers may check the Refs. [34,85].

5.2 Complexity factor

In 2018, Herrera [86] introduced the concept of the complexity factor in the context of GR for spherically symmetric and static self-gravitating systems. The core idea behind the complexity factor involves systems that are either simple or minimally complicated, exhibiting homogeneous energy density and isotropic pressure. In static, spherically symmetric spacetimes, Herrera [86] demonstrated that a scalar function naturally emerges from the orthogonal decomposition of the Riemann tensor, capturing essential features of the system's complexity [87,88]. This scalar quantity, referred to as the *complexity factor* and denoted by Υ_{TF}, enclose the contributions from pressure anisotropy and energy density inhomogeneity, and is given by

$$\Upsilon_{TF} = 8\pi\tau - \frac{4\pi}{r^3}\int_0^r \tilde{r}^3\rho'(r)d\tilde{r}, \tag{46}$$

where $\tau = p_r - p_t$ represents the difference between radial pressure and transverse pressure. Additionally, the above expression (46) enables the representation of the Tolman mass as

$$m_T = (m_T)_\Sigma\left(\frac{r}{r_\Sigma}\right)^3 + r^3\int_0^{r_\Sigma}\frac{e^{(\xi+\lambda)/2}}{\tilde{r}}\Upsilon_{TF}d\tilde{r}, \tag{47}$$

This formulation highlights how the complexity factor directly influences the active gravitational mass by integrating the combined effects of matter distribution and anisotropic pressures. Importantly, the condition for zero complexity, $\Upsilon_{TF} = 0$, is not limited to isotropic and homogeneous systems. It can also be satisfied in cases where

$$\tau = \frac{1}{2r^3}\int_0^r \tilde{r}^3\rho'(r)d\tilde{r}. \tag{48}$$

In this scenario, the vanishing complexity condition leads to a non-local equation of state, providing an additional constraint needed to complete the system of Einstein's field equations. Recent works have examined this methodology extensively, as highlighted in Refs. [89–91]. In the present study, we explore the behavior of the complexity factor associated with wormhole configurations in galactic environments. Given that wormholes are typically defined over the radial domain $r_0 \leq r < \infty$, it becomes necessary to appropriately adapt the complexity factor expression (46) to accommodate this setting. The modified expression for the complexity factor is given by

$$\Upsilon_{TF} = 8\pi\tau - \frac{4\pi}{r^3}\int_{r_0}^{r} \tilde{r}^3\rho'(r)d\tilde{r}. \tag{49}$$

Although the standard formulation assumes $r_0 = 0$, this particular scenario is excluded to ensure that the wormhole throat maintains a finite size.

We have analyzed the evolution of the complexity factor for three dark matter-supported wormhole configurations, and the corresponding behavior is illustrated in Figs. 4. Our analysis reveals that the complexity factor Υ_{TF} exhibits an asymptotic behavior but gradually vanishes and approaches zero as the radial coordinate increases, i.e., in the limit $r \to \infty$, corresponding to regions far from the wormhole throat. As discussed in [86], a minimal value of the complexity factor typically indicates a system with a uniform energy density and isotropic pressure. On the other hand, a vanishing complexity factor can also emerge in scenarios where the effects of energy density inhomogeneity and pressure anisotropy precisely compensate for each other. Close to the throat $r = r_0$, the complexity factor decreases monotonically, but as we extend the radial coordinate, Υ_{TF} gradually declines and approaches zero. This trend is consistently observed in all values tested for the model parameter $\beta > 0$. Therefore, in the context of wormhole geometries within galactic halos governed by $f(R, \mathcal{L}_m, T)$ gravity, the complexity factor naturally converges to zero at large radial distances, particularly when β is positive. It is also noteworthy that, within the framework of complexity analysis, pressure anisotropy plays a more significant role than energy density homogeneity. For further insights on this topic, the reader is referred to recent developments discussed in [92–94].

5.3 Anisotropy parameter

The geometry and stability of wormholes are deeply affected by the presence of pressure anisotropy, which plays a pivotal role in determining their traversability. A valuable tool in characterizing this anisotropy is the dimensionless parameter Δ, defined as [95]

$$\Delta = \frac{p_t - p_r}{\rho}. \tag{50}$$

According to the analysis presented in Ref. [59], a positive anisotropy ($\Delta > 0$) implies a repulsive effect within the geometry, leading to an outward-directed force. In contrast, a negative anisotropy ($\Delta < 0$) enhances the inward gravitational attraction, contributing to a more attractive geometry. This behavior highlights the critical role of anisotropic stresses in shaping the physical and geometrical features of wormhole spacetimes. Keeping this in mind, we investigated the behavior of the anisotropy parameter in Fig. 5. It was observed that Δ showed positive behavior in all cases, resulting in repulsive behavior of the wormhole solutions.

5.4 Active gravitational mass

The active gravitational mass enclosed within a wormhole, measured from the throat at r_0 up to a radial boundary R, is given by

$$\mathcal{M}_{\mathcal{A}} = 4\pi\int_{r_0}^{R}\rho(r)r^2dr, \tag{51}$$

where $\mathcal{M}_{\mathcal{A}}$ represents the active mass function. A positive value of this quantity is generally interpreted as an indicator of physical viability for the wormhole model under consideration. In this context, we explore three different dark matter halo models and determine the conditions under which the active mass function remains positive. For the URC model (15), the corresponding expression for the active gravitational mass becomes

$$\mathcal{M}_{\mathcal{A}} = \pi\rho_s r_s^3\left[\log\left(r_s^2+R^2\right) - \log\left(r_s^2+r_0^2\right) + 2\Omega - 2\tan^{-1}\left(\frac{R}{r_s}\right) + 2\tan^{-1}\left(\frac{r_0}{r_s}\right)\right], \tag{52}$$

where $\Omega = \log(r_s + R) - \log(r_s + r_0)$. For the NFW model, the mass function is expressed as

$$\mathcal{M}_{\mathcal{A}} = 4\pi\rho_s r_s^3\left(\frac{r_s}{r_s+R} + \Omega - \frac{r_s}{r_s+r_0}\right). \tag{53}$$

Finally, for the PI case, we obtain

$$\mathcal{M}_{\mathcal{A}} = 4\pi\rho_s r_s^2\left(-r_s\tan^{-1}\left(\frac{R}{r_s}\right) + r_s\tan^{-1}\left(\frac{r_0}{r_s}\right) + R - r_0\right). \tag{54}$$

We now examine the behavior of the active gravitational mass $\mathcal{M}_A$ for each dark matter model in the context of the wormhole geometry, as illustrated in Fig. 6. As previously noted, a positive gravitational mass indicates a physically viable configuration. From Fig. 6, it is evident that $\mathcal{M}_A$ remains positive throughout, thereby confirming the physical acceptability of the proposed models [96].

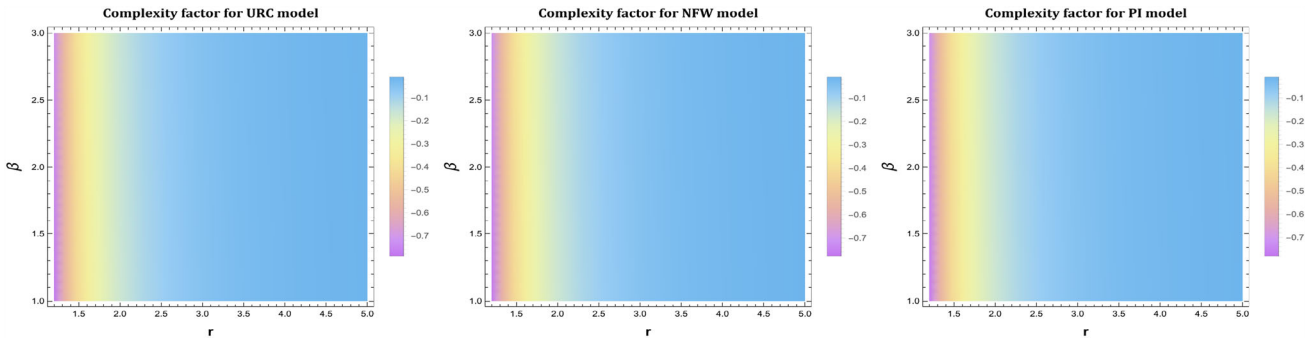

Fig. 4 The plots for the complexity factor $\Upsilon_{TF}(r,\ \beta)$ against the radial coordinate r and model parameter β. We consider the parameter values $\rho_s = 0.004\,\text{kpc}^{-2}$, $r_s = 2\,\text{kpc}$, throat radius $r_0 = 1\,\text{kpc}$ and $\alpha = 2$

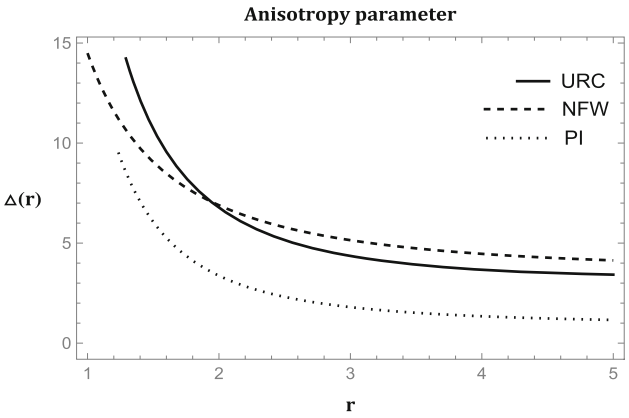

Fig. 5 The variation of anisotropy parameter $\triangle$ against the radial distance r. We consider the parameter values $\rho_s = 0.004\,\text{kpc}^{-2}$, $r_s = 2\,\text{kpc}$, throat radius $r_0 = 1\,\text{kpc}$, $\alpha = 2$ and $\beta = 2$

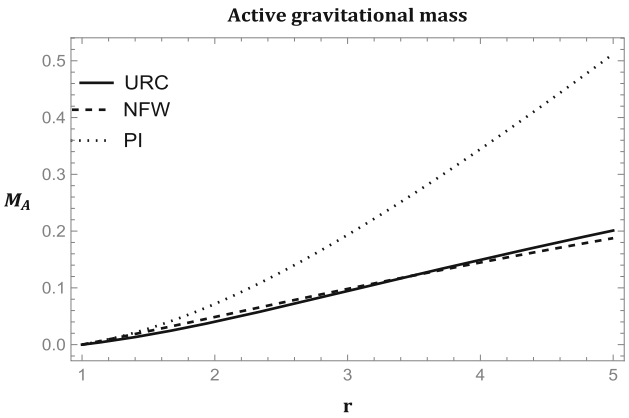

Fig. 6 The variation of active mass $\mathcal{M}_{\mathcal{A}}$ against the radial distance r. We consider the parameter values $\rho_s = 0.004\,\text{kpc}^{-2}$, $r_s = 2\,\text{kpc}$, throat radius $r_0 = 1\,\text{kpc}$, and upper limit $R = 5$

5.5 Total gravitational energy

It has been established that the matter sustaining the wormhole structure violates the NEC, indicating the presence of exotic matter rather than ordinary baryonic matter. The total gravitational energy is typically negative for systems composed of standard baryonic matter. Hence, analyzing the nature of gravitational energy in the context of a wormhole becomes particularly important. Following the methodology proposed by Lyndell-Bell et al. [97] and later extended by Nandi et al. [98], we analyze the total gravitational energy related to galactic wormholes supported by dark matter. The total gravitational energy, denoted by $\mathcal{E}_g$, is expressed as [98]

$$\mathcal{E}_g = \mathcal{M}c^2 - \mathcal{E}_M, \tag{55}$$

where $\mathcal{M}c^2$ corresponds to the total energy and can be calculated using

$$\mathcal{M}c^2 = \frac{1}{2}\int_{r_0}^{r} T_0^0 r^2 dr + \frac{r_0}{2}, \tag{56}$$

with the term $\frac{r_0}{2}$ representing a contribution to the effective mass [98]. The quantity $\mathcal{E}_M$ encloses various forms of energy, such as rest mass, kinetic, and internal energies, and is defined by

$$\mathcal{E}_M = \frac{1}{2}\int_{r_0}^{r} T_0^0 (g_{rr})^{\frac{1}{2}} r^2 dr, \quad \text{with} \quad g_{rr} = \left(1 - \frac{b(r)}{r}\right)^{-1} \tag{57}$$

This expression for $\mathcal{E}_M$ is consistent with the geometric energy definition described by Wald [99]. Notably, since the proper radial distance is greater than the corresponding Euclidean distance, $(g_{rr})^{1/2} > 1$. Consequently, if $T_0^0 > 0$, the condition $\mathcal{E}_g < 0$ indicates attractive gravitational behavior; conversely, if $T_0^0 < 0$, then $\mathcal{E}_g > 0$, implying repulsion [100]. Given the complexity of the integrals in Eq. (55), we evaluate them numerically over the range from the wormhole throat (r_0) to the specified radial embedding of the spacetime geometry, as detailed in Table 1. The results, illustrated in Fig. 7, reveal that $\mathcal{E}_g > 0$ near the throat, highlighting a repulsive gravitational character. Interestingly, this outcome arises even when $T_0^0 > 0$, which can be attributed to the exotic nature of the matter violating the NEC. Comparable findings regarding the repulsive behavior of $\mathcal{E}_g$ have also been reported in [96,101]. This repulsive gravitational

Table 1 The table presents the numerical values of $\mathcal{E}_g$ corresponding to various DM models. We consider the parameter values $\rho_s = 0.004\,\text{kpc}^{-2}$, $r_s = 2\,\text{kpc}$, $r_0 = 1\,\text{kpc}$, $\alpha = 2$ and $\beta = 2$

The numerical values of $\mathcal{E}_g$ for different r			
r	URC	NFW	PI
1.5	0.498659	0.497957	0.497812
2.0	0.498101	0.497329	0.496674
2.5	0.497667	0.496905	0.495604
3.0	0.49731	0.496583	0.494544
3.5	0.497008	0.496324	0.493477
4.0	0.49675	0.496108	0.492397
4.5	0.496526	0.495925	0.491303
5.0	0.49633	0.495766	0.490194

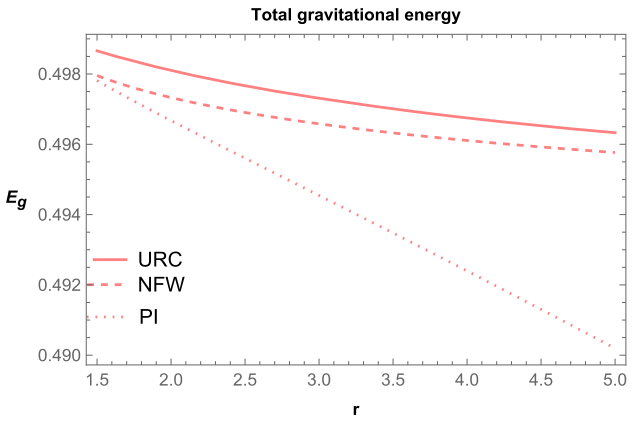

Fig. 7 The variation of $\mathcal{E}_g$ against the radial distance r. We consider the parameter values $\rho_s = 0.004\,\text{kpc}^{-2}$, $r_s = 2\,\text{kpc}$, throat radius $r_0 = 1\,\text{kpc}$, $\alpha = 2$ and $\beta = 2$

energy is consistent with the physical requirements to sustain a traversable wormhole (Table 1).

5.6 The emergence of exotic matter

The volume integral quantifier (VIQ) serves as a valuable tool for estimating the total quantity of matter that violates the averaged null energy condition (ANEC) within a given spacetime structure [102]. In the context of wormhole physics, it measures the overall amount of exotic matter necessary to sustain the wormhole structure. This is executed by evaluating the volume integral

$$I_V = \oint [\rho(r) + p_r(r)]\, dV = 2\int_{r_0}^{\infty} [\rho(r) + p_r(r)]\, dV, \tag{58}$$

which, in spherical symmetry, simplifies to

$$I_V = 8\pi \int_{r_0}^{\infty} [\rho(r) + p_r(r)]\, r^2\, dr, \tag{59}$$

using the standard volume element $dV = 4\pi r^2 dr$. To compute this integral for our specific shape function $b(r)$, we restrict the domain of integration to a finite region, recognizing that the contribution from regions far from the wormhole throat becomes negligible and that suitable interest lies near the throat itself [59]. Introducing a finite upper bound $r_1 > r_0$, we redefine the VIQ as

$$I_V = 8\pi \int_{r_0}^{r_1} [\rho(r) + p_r(r)]\, r^2\, dr. \tag{60}$$

This formulation allows us to quantify the localized existence of exotic matter and evaluate the physical viability of the wormhole structure within a finite spatial domain. It is important to note that as $r_1 \to r_0$, the VIQ satisfies the condition $I_V \to 0$ [102]. Based on this, we have plotted the behavior of I_V for each dark matter model, as shown in Fig. 8. The plots indicate that I_V remains negative for all $r_1 > r_0$. However, as r_1 approaches the wormhole throat radius r_0, the value of I_V asymptotically tends to zero, i.e., $I_V \to 0$ as $r_1 \to r_0$. This behavior supports spacetime geometries that accommodate traversable wormholes that require arbitrarily small amounts of exotic matter. Therefore, the overall amount of matter that violates the ANEC can be optimized by selecting a suitable wormhole structure. For a more detailed discussion of this topic, we refer the reader to Refs. [103–105].

6 Conclusions

This paper explores the intriguing domain of traversable wormholes within the framework of $f(R, \mathcal{L}_m, T)$ gravity, an extension of conventional gravitational theories that incorporates the Lagrangian matter and the trace of the energy-momentum tensor. We considered the modified gravity model, which is expressed as $f(R, \mathcal{L}_m, T) = R + \alpha\mathcal{L}_m + \beta T$, where α and β are coupling parameters. Considering $\mathcal{L}_m = -\rho$ and assuming a constant redshift function $\Phi(r)$, we analyze the fundamental properties of wormholes and their stability in the presence of DM models.

We first derive the shape function of wormholes under URC, NFW, and PI DM models and examine their physical behaviors. The asymptotic flatness condition was observed for small values of ρ_s and any choice of model parameters. Furthermore, we find that for higher values of β, the flare-out condition may not be maintained near the wormhole throat. Furthermore, an investigation of the NEC for each case reveals its violation at $r = r_0$, implying the violation of all the energy conditions. However, this violation arises because of the effects of modified gravity, which effectively serves as an alternative source of exotic matter near the throat. Subsequently, we analyzed the stability of the obtained wormhole solutions under various parameters corresponding to the considered DM models. Initially, the gravitational lens-

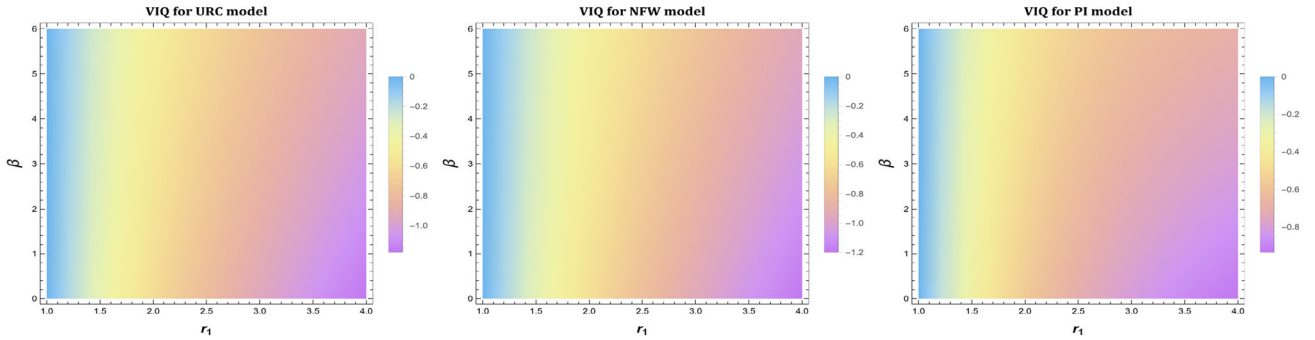

Fig. 8 The plots for the $I_V(r,\ \beta)$ against the radial coordinate r and model parameter β. We consider the parameter values $\rho_s = 0.004\,\text{kpc}^{-2}$, $r_s = 2\,\text{kpc}$, throat radius $r_0 = 1\,\text{kpc}$, and $\alpha = 2$

ing properties of the wormholes were examined, and exact deflection angle expressions were derived using the Gauss–Bonnet theorem. Our findings indicate that both the model parameter β and the impact parameter Ψ significantly influence the deflection behavior. Specifically, for the NFW profile, the deflection angle becomes negative within the range $\beta \in [0, 6]$, implying that photons are deflected outward, away from the wormhole. In contrast, the deflection angle remains positive for the URC and PI models, indicating that light rays bend inward toward the wormhole throat. We further studied the complexity factor introduced by Herrera [86], observing that it naturally tends toward zero at large radial distances, particularly when $\beta > 0$, thereby indicating a less complex configuration in the asymptotic region. Additionally, the anisotropic behavior, using the anisotropy parameter Δ, was evaluated and found to be positive ($\Delta > 0$) in all cases, suggesting a repulsive anisotropic force that contributes to the wormhole's stability. Moreover, we investigated the active gravitational mass $\mathcal{M}_A$ and the total gravitational energy $\mathcal{E}_g$ of the system. The results show that $\mathcal{M}_A$ remains positive for all considered cases, confirming the physical viability of the solutions [96]. The numerical analysis of the gravitational energy reveals that $\mathcal{E}_g$, indicating a repulsive gravitational nature near the throat, a feature consistent with the fundamental requirements for sustaining traversable wormholes. Similar repulsive behavior has also been reported in 4D EGB gravity framework [106]. Finally, the VIQ was employed to estimate the amount of exotic matter required near the throat to support a traversable wormhole. The analysis suggests that only a small amount of exotic matter is necessary, aligning with the findings of Ref. [107]. It is worth mentioning that the present study assumes a zero-tidal-force condition, i.e., $\Phi'(r) = 0$. Future investigations may consider non-constant redshift functions and non-minimal matter-geometry coupling, as explored in Refs. [28,30], to obtain a more generalized and comprehensive understanding of wormhole solutions.

Acknowledgements PKS acknowledges the Ministry of Higher Education (MoHE), Govt. of Malaysia, for the financial support through the Fundamental Research Grant Scheme (FRGS/1/2023/STG07/UM/02/3, project no.: FP074-2023) and IUCAA, Pune, India for providing support through the visiting Associateship program. We are grateful to the honorable referees and the editor for the insightful suggestions and constructive comments that have significantly improved our work in terms of research quality and presentation.

Data Availability Statement There are no new data associated with this article. [Authors' comment: Data sharing not applicable to this article as no datasets were generated or analysed during the current study.]

Code Availability Statement This manuscript has no associated code/software. [Authors' comment: Code/Software sharing not applicable to this article as no code/software was generated or analysed during the current study.]

Funded by SCOAP[3].

References

1. A. Einstein, N. Rosen, Phys. Rev. **48**, 73 (1935)
2. C.W. Misner, J.A. Wheeler, Ann. Phys. **2**, 525 (1957)
3. M.S. Morris, K.S. Thorne, Am. J. Phys. **56**, 395 (1988)
4. M.S. Morris, K.S. Thorne, U. Yurtsever, Phys. Rev. Lett. **61**, 1446 (1988)
5. M. Visser, *Lorentzian Wormholes: From Einstein to Hawking* (AIP Press, New York, 1995)
6. H.G. Ellis, J. Math. Phys. **14**, 104 (1973)
7. H.G. Ellis, Gen. Relativ. Gravit. **10**, 105 (1979)
8. B. Kleihaus, J. Kunz, Phys. Rev. D **90**, 121503 (2014)

9. G. Clement, Gen. Relativ. Gravit. **16**, 131–138 (1984)
10. A. DeBenedictis, A. Das, Nuclear Phys. B **653**, 279 (2003)
11. J.W. Moffat, T. Svoboda, Phys. Rev. D **44**, 429 (1991)
12. G. Antoniou, A. Bakopoulos, P. Kanti, B. Kleihaus, J. Kunz, Phys. Rev. D **101**, 024033 (2020)
13. P. Kanti, B. Kleihaus, J. Kunz, Phys. Rev. D **85**, 044007 (2012)
14. K.A. Bronnikov, A.M. Galiakhmetov, Phys. Rev. D **94**, 124006 (2016)
15. M.R. Mehdizadeh, A.H. Ziaie, Phys. Rev. D **99**, 064033 (2019)
16. M. Zubair, S. Waheed, Y. Ahmad, Eur. Phys. J. C **76**, 444 (2016)
17. R. Solanki, Z. Hassan, P.K. Sahoo, Chin. J. Phys. **85**, 74 (2023)
18. S. Halder, S. Bhattacharya, S. Chakraborty, Mod. Phys. Lett. A **34**, 1950095 (2019)
19. I.P. Lobo, M.G. Richarte, J.P.M. Grac, H. Moradpour, Eur. Phys. J. Plus **135**, 550 (2020)
20. Y. Heydarzade, M. Ranjbar, Eur. Phys. J. Plus **138**, 703 (2023)
21. R. Shaikh, Phys. Rev. D **92**, 024015 (2015)
22. R. Rahaman, N. Paul, A. Banerjee, S.S. De, S. Ray, A.A. Usmani, Eur. Phys. J. C **76**, 246 (2016)
23. S. Kiroriwal, J. Kumar, S.K. Maurya, S. Chaudhary, Eur. Phys. J. C **84**, 414 (2024)
24. M. Ilyas, K. Bamba, J. Cosmol. Astropart. Phys. **2023**, 038 (2023)
25. N. Kavya, V. Venkatesha, G. Mustafa, P.K. Sahoo, Ann. Phys. **455**, 169383 (2023)
26. M. Tayde, Z. Hassan, P.K. Sahoo, Phys. Dark Univ. **42**, 101288 (2023)
27. G. Mustafa, Z. Hassan, P.K. Sahoo, Class. Quantum Gravity **41**, 235001 (2024)
28. Z. Haghani, T. Harko, Eur. Phys. J. C **81**, 615 (2021)
29. J.G. de Lima Jr, P.H.R.S. Moraes, E. Brito, J.A.S. Fortunato, Eur. Phys. J. C **85**, 38 (2025)
30. D.C. Maurya, Phys. Dark Univ. **46**, 101722 (2024)
31. J.S. Goncalves, A.F. Santos, Nucl. Phys. B **1010**, 116751 (2025)
32. P.H.R.S. Moraes et al., Phys. Lett. B **855**, 138818 (2024)
33. N. Loewer, M. Tayde, P.K. Sahoo, Eur. Phys. J. C **84**, 1196 (2024)
34. A. Errehymy et al., J. High Energy Astrophys. **47**, 100370 (2025)
35. Z. Hassan, S. Hossain, S.N. Barman, P.K. Sahoo, Eur. Phys. J. C **85**, 754 (2025)
36. Planck Collaboration: P.A.R. Ade et al., A&A **594**, A13 (2016)
37. Planck Collaboration: N. Aghanim et al., A&A **641**, A6 (2020)
38. S. Trujillo-Gomez, A. Klypin, J. Primack, A.J. Romanowsky, Astrophys. J. **742**, 16 (2011)
39. F. Zwicky, Astrophys. J. **86**, 217 (1937)
40. M.S. Roberts, Astrophys. J. **83**, 1026 (1978)
41. L. Roszkowski, E.M. Sessolo, S. Trojanowski, Rep. Prog. Phys. **81**, 066201 (2018)
42. F. Rahaman, P.K.F. Kuhfittig, S. Ray, N. Islam, Eur. Phys. J. C **74**, 2750 (2014)
43. F. Rahaman, P. Salucci, P.K.F. Kuhfittig, S. Ray, M. Rahaman, Ann. Phys. **350**, 561 (2014)
44. K.G. Begeman, A.H. Broeils, R.H. Sanders, Mon. Not. R. Astron. Soc. **249**, 523 (1991)
45. M. Milgrom, Phys. Rev. Lett. **117**, 141101 (2016)
46. M. Milgrom, Astrophys. J. **270**, 365 (1983)
47. M. Milgrom, Astrophys. J. **270**, 371 (1983)
48. W.J.G. de Blok, S.S. McGaugh, A. Bosma, V.C. Rubin, Astrophys. J. **552**, L23–L26 (2001)
49. B.C. Paul, Class. Quantum Gravity **38**, 145022 (2021)
50. A. Errehymy, Y. Khedif, O. Donmez, M. Daoud, K. Myrzakulov, S. Bekov, Eur. Phys. J. C **84**, 908 (2024)
51. C.R. Muniz, R.V. Maluf, Ann. Phys. **446**, 169129 (2022)
52. H. Nazar et al., Phys. Dark Univ. **48**, 101837 (2025)
53. P. Das, M. Kalam, Eur. Phys. J. C **82**, 342 (2022)
54. L. Herrera, N.O. Santos, Phys. Rep. **286**, 53 (1997)
55. L. Herrera, Phys. Rev. D **101**, 104024 (2020)
56. F.S.N. Lobo, Phys. Rev. D **71**, 084011 (2005)
57. M.R. Mehdizadeh, M.K. Zangeneh, F.S.N. Lobo, Phys. Rev. D **91**, 084004 (2015)
58. M. Cataldo, S. del Campo, Phys. Rev. D **85**, 104010 (2012)
59. F.S.N. Lobo, F. Parsaei, N. Riazi, Phys. Rev. D **87**, 084030 (2013)
60. S. Halder, S. Bhattacharya, S. Chakraborty, Phys. Lett. B **791**, 270–275 (2019)
61. P.K.F. Kuhfittig, Eur. Phys. J. C **74**, 2818 (2014)
62. J.H. Oort, Bull. Astron. Inst. Neth. **3**, 275 (1927)
63. F. Zwicky, Helv. Phys. Acta **6**, 110 (1933)
64. J.F. Navarro, C.S. Frenk, S.D.M. White, Astrophys. J. **462**, 563 (1996)
65. J.F. Navarro, C.S. Frenk, S.D.M. White, Astrophys. J. **490**, 493 (1997)
66. D. Merritt et al., Astron. J. **624**, L85 (2005)
67. D. Merritt et al., Astron. J. **132**, 2685 (2006)
68. A. Burkert, Astron. J. **447**, L25–L28 (1995)
69. P. Salucci, A. Burkert, Astrophys. J. **537**, L9 (2000)
70. G. Gentile, P. Salucci, U. Klein, D. Vergani, P. Kalberla, Mon. Not. Roy. Astron. Soc. **351**, 903 (2004)
71. P. Salucci, I.A. Yegorova, N. Drory, Mon. Not. Roy. Astron. Soc. **388**, 159 (2008)
72. M. Spano, M. Marcelin, P. Amram, C. Carignan, B. Epinat, O. Hernandez, Mon. Not. Roy. Astron. Soc. **383**, 297 (2007)
73. C.F. Martins, P. Salucci, Phys. Rev. Lett. **98**, 151301 (2007)
74. M. Persic, P. Salucci, F. Stel, Mon. Not. Roy. Astron. Soc. **281**, 27 (1996)
75. S. Sarkar, N. Sarkar, F. Rahaman, Eur. Phys. J. C **80**, 882 (2020)
76. J. Dubinski, R.G. Carlberg, Astron. J. **378**, 496 (1991)
77. F. Governato et al., Nature **463**, 203–206 (2010)
78. A.A. Dutton, A.V. Maccio, Mon. Not. Roy. Astron. Soc. **441**, 3359 (2014)
79. S.-H. Oh, W.J.G. de Blok, E. Brinks, F. Walter, R.C. Kennicutt Jr., Astron. J. **141**, 193 (2011)
80. Z. Xu, M. Tang, G. Cao, S.-N. Zhang, Eur. Phys. J. C **80**, 70 (2020)
81. M.K. Zangeneh, F.S.N. Lobo, N. Riazi, Phys. Rev. D **90**, 024072 (2014)
82. A. Jawad, S. Rani, Eur. Phys. J. C **76**, 704 (2016)
83. G.C. Samanta, N. Godani, Eur. Phys. J. C **79**, 623 (2019)
84. G. Gibbons, M. Werner, Class. Quantum Gravity **25**, 235009 (2008)
85. A. Ovgun, G. Gyulchev, K. Jusufi, Ann. Phys. **406**, 152–172 (2019)
86. L. Herrera, Phys. Rev. D **97**, 044010 (2018)
87. Alfonso Garcia-Parrado Gomez-Lobo, Class. Quantum Gravity **25**, 015006 (2008)
88. L. Herrera et al., Phys. Rev. D **79**, 064025 (2009)
89. R. Casadio et al., Eur. Phys. J. C **79**, 826 (2019)
90. E. Contreras, E. Fuenmayor, Phys. Rev. D **103**, 124065 (2021)
91. C. Arias, E. Contreras, E. Fuenmayor, A. Ramos, Ann. Phys. **436**, 168671 (2022)
92. M. Sharif, I.I. Butt, Eur. Phys. J. C **78**, 688 (2018)
93. Z. Yousaf, M.Y. Khlopov, M.Z. Bhatti, T. Naseer, MNRAS **495**, 4334–4346 (2020)
94. M. Zubair, M. Farooq, Eur. Phys. J. C **83**, 507 (2023)
95. C. Cattoen, T. Faber, M. Visser, Class. Quantum Gravity **22**, 4189 (2005)
96. P. Bhar, F. Rahaman, T. Manna, A. Banerjee, Eur. Phys. J. C **76**, 708 (2016)
97. D. Lynden-Bell, J. Katz, J. Bicak, Phys. Rev. D **75**, 024040 (2007)
98. K.K. Nandi, Y.Z. Zhang, R.G. Cai, A. Panchenko, Phys. Rev. D **79**, 024011 (2009)
99. R.M. Wald, *General Relativity* (University of Chicago Press, Chicago, 1984)
100. C.W. Misner, K.S. Thorne, J.A. Wheeler, *Gravitation* (Freeman, San Francisco, 1973), pp.467–603

101. F. Rahaman, S. Karmakar, I. Karar, S. Ray, Phys. Lett. B **746**, 73–78 (2015)
102. M. Visser, S. Kar, N. Dadhich, Phys. Rev. Lett. **90**, 201102 (2003)
103. K. Jusufi, M. Jamil, M. Rizwan, Gen. Relativ. Gravit. **51**, 102 (2019)
104. O. Sokoliuk, S. Mandal, P.K. Sahoo, A. Baransky, Eur. Phys. J. C **82**, 280 (2022)
105. M.M. Rizwan, Z. Hassan, P.K. Sahoo, A. Ovgun, Eur. Phys. J. C **84**, 1132 (2024)
106. Z. Hassan, P.K. Sahoo, Ann. Physik **536**, 2400114 (2024)
107. T. Naseer, M. Sharif, M. Faiza, W. Albalawi, A.-H.A. Aty, Phys. Dark. Univ. **48**, 101890 (2025)